A&A, 688, A138 (2024)
https://doi.org/10.1051/0004-6361/202349042

Astronomy & Astrophysics

Magnetohydrodynamic simulations of the space weather in Proxima b: Habitability conditions and radio emission⋆

L. Peña-Moñino[1], M. Pérez-Torres[1,2,3], J. Varela[4,5], and P. Zarka[6,7]

[1] CSIC, Instituto de Astrofísica de Andalucía, Glorieta de la Astronomía S/N, 18008, Granada, Spain
e-mail: lpm@iaa.es; torres@iaa.es
[2] Center for Astroparticles and High Energy Physics (CAPA), Universidad de Zaragoza, 50009 Zaragoza, Spain
[3] School of Sciences, European University Cyprus, Diogenes street, Engomi, 1516 Nicosia, Cyprus
[4] Universidad Carlos III de Madrid, 28911, Leganés, Spain
e-mail: jvrodrig@fis.uc3m.es
[5] Institute for Fusion Studies, University of Texas, Austin, TX 78712, USA
[6] LESIA, Observatoire de Paris, CNRS, PSL, SU/UPD, Meudon, France
[7] USN, Observatoire de Paris, CNRS, PSL, UO, Nançay, France

Received 20 December 2023 / Accepted 9 May 2024

ABSTRACT

Context. The habitability of exoplanets hosted by M dwarf stars dramatically depends on the space weather, where the magnetic and ram pressure of the stellar wind, and the exoplanet magnetic field are the three main players. These three parameters also likely drive the radio emission arising close to the planet.
Aims. Our aim is to characterize the magneto-plasma environment and thus the habitability of the Earth-like planet Proxima b, which is inside the habitable zone of its host M dwarf star Proxima, when it is subject to average calm space weather conditions, and to more extreme space weather conditions, for example a coronal mass ejection (CME) event. We study the role of the stellar wind and planetary magnetic field, and their mutual orientation. We also determine the radio emission arising from the interaction between the stellar wind of Proxima and the magnetosphere of its planet Proxima b, which is relevant to guiding radio observations aimed at unveiling planets.
Methods. We used the PLUTO code to run a set of 3D magneto-hydrodynamic simulations focused on the space weather around planet Proxima b. We considered both calm and space weather conditions for Proxima b, under three different scenarios: (a) Proxima b subject to calm space weather in a sub-Alfvénic regime, where the stellar wind magnetic pressure dominates over the wind's ram pressure; (b) Proxima b subject to calm space weather in a super-Alfvénic regime, where the ram pressure of the wind dominates, and a bow shock is formed; and (c) Proxima b subject to a coronal mass ejection event, when the dynamical and magnetic pressure of the stellar wind from its host star are increased enormously for a short period of time.
Results. We find that if Proxima b has a magnetic field similar to that of the Earth ($B_p = B_\oplus \approx 0.32$ G) or larger, the magnetopause standoff distance is large enough to shield the surface from the stellar wind for essentially any planetary tilt but the most extreme values (close to 90°) under a calm space weather. Even if Proxima b is subject to more extreme space weather conditions, for example a CME event from its host star, the planet is well shielded by an Earth-like magnetosphere ($B_p \approx B_\oplus$; $i \approx 23.5°$), or if it has a tilt smaller than that of the Earth. Otherwise, the planetary magnetic field must be larger to shield the planet from particle precipitation on the surface. For calm space weather conditions, the radio emission caused by the day-side reconnection regions can be as high as 7×10^{19} erg s^{-1} in the super-Alfvénic regime, and is on average almost an order of magnitude larger than the radio emission in the sub-Alfvénic cases, due to the much larger contribution of the bow shock, which is not formed in the sub-Alfvénic regime. We also find that the energy dissipation at the bow shock is essentially independent of the angle between the planet's magnetic dipole and the incident stellar wind flow. If Proxima b is subject to extreme space weather conditions, the radio emission is more than two orders of magnitude larger than when under calm space weather conditions. This result yields expectations for a direct detection (from Earth) in radio of giant planets in close-in orbits as they are expected to have magnetic fields large enough, so that their electron-cyclotron frequency exceeds the ionosphere cutoff.

Key words. magnetic reconnection – magnetohydrodynamics (MHD) – planets and satellites: magnetic fields – planetary systems

1. Introduction

The space weather of exoplanets depends on the properties of the stellar wind, mainly through its density (n_{sw}), velocity (v_{sw}), and magnetic field (B_{IMF}), and on the magnetic field of the planet (B_p). If the exoplanet orbit is located in the inner part of the habitable zone, extreme conditions or the absence of a significant magnetic field can lead to direct deposition of the stellar wind toward the exoplanet surface, thus threatening the planet habitability (Varela et al. 2022b). In the case of the Earth, whose host star is a G-type star, its magnetic field is strong enough to avoid the direct precipitation of the damaging particles and high-energy radiation from the solar wind on the surface, even during the largest coronal mass ejections (CMEs) observed (Kilpua et al. 2019; Hapgood 2019). CMEs are stellar eruptions produced by magnetic reconnections in the stellar corona (Low 2001), which expel a magnetic cloud of charged paticles moving at a

⋆ The movies associated to Fig. 2 are available at https://www.aanda.org

few times the wind speed (thousands of km s^{-1}) (Neugebauer & Goldstein 1997). Extreme space weather events are not exclusive of Sun-like stars, and have also been observed in M-, K-, and F-type stars (Khodachenko et al. 2007; Lammer et al. 2007).

The space weather around exoplanets cannot be directly compared to the case of the Earth if the host star has characteristics different from the Sun (e.g., stellar type, age, metallicity, magnetic field, rotation). If the dynamic pressure, $P_{\rm d}$, and the magnetic pressure, $P_{\rm IMF}$, of the stellar wind are large, favorable exoplanet habitability conditions necessarily require an intrinsic exoplanet magnetic field strong enough to prevent the direct precipitation of the stellar wind on the exoplanet surface (e.g., Airapetian et al. 2020 and references therein). Otherwise, if the exoplanetary magnetic field is not strong enough, the exoplanet habitability will be hampered by the effect of the stellar wind, as well as the depletion of the atmosphere, especially volatile components such as water molecules (Jakosky et al. 2015), although the role of the planetary magnetic field versus atmospheric escape may be more complex than a simple shield (Gronoff et al. 2020).

Space weather conditions inside the stellar habitable zone depend on the characteristics of the host star (e.g., Airapetian et al. 2020). For M dwarf stars ($< 0.5 M_{Sun}$) the habitable zone is between 0.03 and 0.25 au (Shields et al. 2016). The habitability conditions on exoplanets inside the habitable zone of M dwarf stars are still an open issue. First, those exoplanets are likely to be tidally locked (Grießmeier et al. 2004) and exposed to a strong radiation from the host star (Grießmeier et al. 2005; Scalo et al. 2007) as well as persistent CME events. On the other hand, recent studies indicate that tidal locking may constrain, but not preclude, the habitability conditions of exoplanets (Barnes 2017). Second, space weather conditions also change with the rotation rate of the star because the magnetic activity and the properties of the stellar wind generated by the star change (Suzuki 2013).

The interaction of the stellar wind with an exoplanetary magnetosphere results in the formation of magnetospheric reconnection regions. The dissipation of energy at the magnetopause or, in a super-Alfvénic regime, at the bow shock, leads to indirect or direct electron acceleration (e.g., direct acceleration driven by a Dungey-like cycle; Dungey 1961). Those accelerated electrons precipitate toward the central magnetized body (the planet in the case of magnetospheric emission; most likely the star in the case of sub-Alfvénic star-planet interaction). Eventually, the precipitating electrons are responsible for the emission at cyclotron radio frequencies near the magnetized body. This radio emission happens either indirectly, via the loss-cone emission (Wu & Lee 1979), where the emitting electrons are the ones reflected at their mirror points, or directly, for example via beam or shell emission (e.g., Hess et al. 2008).

The mechanism behind this radio emission is the electron-cyclotron maser instability (Wu & Lee 1979), which is responsible for the low-frequency emission seen from the interaction of the solar wind with planets in the Solar System with intrinsic magnetic fields, for example Jupiter (Kaiser & Desch 1984; Zarka 1998), where a fraction of the electron energy is transformed into cyclotron radio emission escaping from the magnetosphere. Likewise, the radio emission detected from an exoplanet magnetosphere could provide information of the exoplanet intrinsic magnetic field (Hess & Zarka 2011). Unfortunately, the detection capability of present radio telescopes can barely distinguish the radio emission from exoplanets. Recently, different observations have shown tentative detections of radio emission from confirmed star–planet systems, for example Proxima–Proxima b, using the ATCA (Pérez-Torres et al. 2021); Tau Boo–Tau Boo b, using the LOFAR telescope (Turner et al. 2021); and YZ Cet–YZ Cet b, using the VLA (Pineda & Villadsen 2023) and the GMRT (Trigilio et al. 2023). In addition, Vedantham et al. (2020) interpreted LOFAR observations of the red dwarf GJ 1151 as being due to the magnetic star-planet interaction with a putative, yet undiscovered, exoplanet. Unfortunately, none of the above cases have shown conclusive evidence of the radio emission arising from star-planet interaction (Proxima, GJ 1151, YZ Cet) or directly from the planet's magnetosphere (Tau Boo).

We carried out our study using the single fluid magnetohydrodynamics (MHD) code PLUTO in spherical 3D coordinates (Mignone et al. 2007). We have already applied this numerical framework to model global structures of the Hermean magnetosphere (Varela et al. 2015, 2016b,c,a), the effect of an interplanetary CME-like space weather conditions on the Earth magnetosphere (Varela et al. 2022a, 2023), slow modes in the Hermean magnetosphere (Varela et al. 2016d, 2022a), and the radio emission from the Hermean and exoplanetary magnetospheres (Varela et al. 2016e, 2018, 2022b; Mishra et al. 2023).

Proxima Centauri is an M dwarf star, and the closest to our Sun. It is fully convective and slowly rotating ($P_{\rm rot} \sim 84$ days; Suárez Mascareño et al. 2016), with a large-scale magnetic field estimated between ~200 G (Klein et al. 2021) and ~650 G (Reiners & Basri 2008), which seems to have a magnetic cycle of about 7 yr (Suárez Mascareño et al. 2016). Since Proxima b is in the habitable zone of its host star, at a separation of 0.049 au and with an excentricity of 0.02, the stellar activity level is expected to have a crucial influence on the actual planet habitability (e.g., Cohen et al. 2014). Although Proxima is a slow rotator, and is therefore less active than other faster rotating M dwarf stars, it has still significant levels of activity. M dwarfs exhibit in general high levels of activity, with fast-rotating M dwarfs being more active than slow-rotating stars, such as Proxima. For example, Ribas et al. (2016) found that Proxima b receives 30 times more extreme-UV radiation than Earth and 250 times more X-rays. We note, though, that this is essentially due to the large difference in the star-planet separation of Proxima–Proxima b compared to that of the Sun-Earth, which is over 20 times larger. If corrected for the different distance dilution factors, the extreme UV and X-ray irradiation of Proxima b would be factors of ~14 and ~2 smaller, respectively, compared to that of the Earth, as the quiescent X-ray and extreme-UV luminosities of Proxima are smaller than those of the Sun.

The planet Proxima b is an Earth-like planet that lies inside the habitable zone of its host M dwarf star Proxima Centauri (Anglada-Escudé et al. 2016). It may be subject to the effects of CMEs and stellar energetic events, as indicated by the detection of a type IV burst (Zic et al. 2020), whose occurrence is strongly associated with such energetic phenomena. MHD simulations also indicate the importance of space weather conditions on the habitability of Proxima b, which overall faces a more adverse environment than the Earth (Garraffo et al. 2016; Garcia-Sage et al. 2017; Garraffo et al. 2022). The stellar wind dynamic pressure at the orbit of Proxima b can be up to three orders of magnitude higher compared to that of the Earth, particularly during extreme space weather conditions. If calm space weather conditions at the Earth and Proxima b are compared, the wind density is around ten times larger and its velocity twice as large at Proxima b. Likewise, the IMF intensity is more than ten times bigger. On the other hand, space weather conditions may affect the habitability of Proxima b, as far as the shielding provided by its planetary magnetosphere is concerned, so as to avoid the

sterilizing effect of the stellar wind on the surface (see Varela et al. 2022b and references therein). Finally, 3D global climate modeling of the atmosphere and water cycle of Proxima b show that its habitability is possible for a very broad range of atmospheric pressures and compositions, and the presence of surface liquid water requires either a large surface inventory of water (a global ocean able to resupply H2O to the dayside by deep circulation) or an atmosphere with a strong enough greenhouse effect that increases surface temperatures above the freezing point of water (Turbet et al. 2016).

Finally, we note that Proxima b is also a primary target for radio studies, and observations with the Australia Telescope Compact Array have suggested that the observed coherent bursting radio emission may arise from sub-Alfvénic magnetic star-planet interaction (Pérez-Torres et al. 2021), although later MHD simulations suggest that Proxima b is likely to lie in the super-Alfvénic regime (Kavanagh et al. 2021).

In this paper, we present a study of both calm and extreme space weather conditions applied to the closest system hosting an Earth-like exoplanet, the Proxima–Proxima b system. In particular, we study the effect of the planetary magnetic field, and of the angle it makes with the incident stellar wind flow, on the habitability of Proxima b. We also study the radio emission that arises from the electrons accelerated in the magnetic reconnection regions.

Our present study follows a methodology similar to that carried out in previous studies dedicated to analyzing the effects of space weather conditions on exoplanet habitability and radio-emission generation from planetary magnetospheres (Varela et al. 2022a,b). We describe the numerical code PLUTO in Sect. 2. In Sect. 3, we apply the PLUTO code to study and discuss the magneto-plasma environment of Proxima b. We provide a detailed comparison between the MHD simulations performed in this work against those published in previous ones on Proxima Cen. We highlight the qualitative differences of our approach compared to those in other works in Sect. 3. We also note the quantitative differences of our work (Table 1) versus the works by others (see Table 2). In Sect. 4, we discuss the habitability conditions of Proxima b, using the magnetopause standoff distance as a proxy, and in Sect. 5 we determine the radio emission that is expected to arise close to Proxima b. Finally, in Sect. 6 we summarize the main results and conclusions from the paper.

2. Magnetohydrodynamic numerical simulations with PLUTO

PLUTO is an open-source, full 3D MHD code in spherical coordinates that computes the evolution of a single-fluid polytropic plasma in the nonresistive and inviscid limit (Mignone et al. 2007). The equations solved in our model are the mass, momentum, magnetic field, and energy conservation equations, for an ideal gas. We show below the equations in conservative form:

$$\frac{\partial \rho}{\partial t} + \nabla \cdot (\rho \mathbf{v}) = 0, \tag{1}$$

$$\frac{\partial \mathbf{m}}{\partial t} + \nabla \cdot \left[\mathbf{m}\mathbf{v} - \frac{\mathbf{B}\mathbf{B}}{4\pi} + I\left(P + \frac{\mathbf{B}^2}{8\pi}\right)\right]^T = 0, \tag{2}$$

$$\frac{\partial \mathbf{B}}{\partial t} + \nabla \times \mathbf{E} = 0, \tag{3}$$

$$\frac{\partial E_t}{\partial t} + \nabla \cdot \left[\left(\frac{\rho \mathbf{v}^2}{2} + \rho e + P\right)\mathbf{v} + \frac{\mathbf{E} \times \mathbf{B}}{4\,\pi}\right] = 0. \tag{4}$$

Here ρ and $\mathbf{v}$ are the plasma density and velocity, $\mathbf{m} = \rho\,\mathbf{v}$ is the momentum density, P is the thermal pressure of the plasma, $\mathbf{B}$ is the magnetic field, $E_t = \rho \mathbf{v}^2/2 + \rho e + B^2/8\pi$ is the total energy density, $\mathbf{E} = -(\mathbf{v} \times \mathbf{B})$ is the electric field, e is the internal energy, and I is the identity tensor. We assume an ideal gas (i.e., $\rho e = P/(\gamma - 1)$) to close the above equations. Here $P = n\,k_B\,T$, where $n = \rho/(\mu m_p)$ is the number density, k_B is the Boltzmann's constant, T is the temperature, and μm_p is the mean mass of the particle. Since we assume a fully ionized proton-electron plasma for the stellar wind, $\mu = 1/2$. The sound speed is $c_{sw} = (\gamma P/\rho)^{1/2}$, where P is the total electron + proton pressure and $\gamma = 5/3$ is the adiabatic index.

We integrate the conservative forms of the equations using a Harten, Lax, Van Leer approximate Riemann solver (`hll`) associated with a diffusive limiter (`minmod`). The initial magnetic fields are divergenceless, and we maintained this condition throughout the simulation, using a mixed hyperbolic/parabolic divergence cleaning technique (Dedner et al. 2002).

The typical setup used in our simulations is as follows. We use a grid of 128 cells in the radial direction, 48 in the polar angle direction, $\theta \in [0, \pi]$, and 96 in the azimuthal angle direction, $\phi \in [0, 2\pi]$. All cells are equidistant in the radial direction. We use a characteristic length in our simulations equal to the size of the exoplanet Proxima b, $L = R_p = 7 \times 10^8$ cm, and a characteristic stellar wind velocity of $V = 10^7$ cm s^{-1}, respectively. The effective numerical magnetic Reynolds number ($R_m = VL/\eta$, where η is the numerical magnetic diffusivity) and the kinetic Reynolds number ($R_e = VL/\nu$, where ν is the numerical viscosity) have values of around 1000. We do not include an explicit value of the dissipation in the model, hence the numerical magnetic diffusivity regulates the typical reconnection in the slow (Sweet–Parker model) regime. A detailed discussion of the numerical magnetic and kinetic diffusivity of the model is provided in Varela et al. (2018).

Our computational domain consists of a thick spherical shell centered around the exoplanet, with the inner boundary set at $R_{in} = 2.2\,R_p$, where R_p is the radius of the planet Proxima b, and the outer boundary $R_{out} = 30\,R_p$. The upper ionosphere model extends between the inner boundary, R_{in}, and $R = 2.5\,R_p$. The upper ionosphere model is based on the electric field generated by the field-aligned currents providing the plasma velocity at the upper ionosphere, and we describe the model in detail in Appendix A. We set a cutoff radius for B_{IMF} of $R_c = 6\,R_p$. This initial value corresponds to the approximate magnetopause standoff distance for the space weather conditions analyzed in this study, and represents the region where the magnetic field of Proxima b is stronger than the interplanetary magnetic field.

We divide the outer boundary in two regions: an upstream region, where we fix the stellar wind parameters, and a downstream region, where we assume the null derivative condition ($\frac{\partial}{\partial r} = 0$) for all fields. Regarding the initial conditions of the simulations, we define a paraboloid with the vertex at the dayside of the planet as $x < A - (y^2 + z^2/B)$, with (x, y, z) the Cartesian coordinates, $A = R_c$ and $B = R_c * \sqrt{R_c}$ where the velocity is null. We adjust the density profile to keep the Alfvén velocity, $v_A = B/\sqrt{\mu_0 \rho_{sw}}$, constant. Here, $\rho_{sw} = n_{sw}\,\mu\,m_p$ is the mass density, n_{sw} is the particle number, and m_p the proton mass. In practice, since some of the simulations had a large interplanetary magnetic field, we used values of v_A in the range $(2.6–5.0) \cdot 10^4$ km s^{-1} (a fixed value for each simulation). We note that this Alfvén speed upper limit is defined in the PLUTO simulations to control the time step of the simulations. Namely, the Alfvén speed value sets the Alfvén time of the simulation,

which is linked to the simulation time step. The larger v_A, the smaller is the time step, which may render the simulations extremely costly, computationally speaking. We emphasize that this condition only applies to the upper ionosphere domain.

Our simulations use a frame where the z-axis is given by the Proxima b magnetic axis pointing to the magnetic north pole, the star-planet line is located in the XZ plane (with $x_{star} > 0$; stellar magnetic coordinates) and the y-axis completed a right handed system. We show in Fig. 1 a sketch of the overall geometry for our numerical simulations, including the M dwarf star Proxima, its planet Proxima b, and the planetary and interplanetary magnetic field lines. We rotate the axis of the (dipolar) magnetic field of the planet Proxima b by 90° in the YZ plane with respect to the grid poles to avoid numerical issues (no special treatment was necessary for the singularity at the magnetic poles). For simplicity, we consider that the (unknown) rotation and magnetic axes of Proxima b coincide. We assume that the rotation axis makes an angle of 23.5° (as for the Earth) with the normal to the orbital plane (the ecliptic). To simulate different inclinations i, we modify the orientation of the interplanetary magnetic field (IMF) and the stellar wind velocity vectors.

Our model reproduces the relevant global magnetosphere structures, such as the magnetosheath and magnetopause, as demonstrated for the case of the Hermean magnetosphere (Varela et al. 2015, 2016b,c), although we acknowledge that it does not resolve the plasma depletion layer as a decoupled global structure from the magnetosheath, since the model lacks the required resolution.

We note that the reconnection between the interplanetary and Earth magnetic field is instantaneous (no magnetic pile-up on the planet dayside) and stronger (enhanced erosion of the planetary magnetic field) because the magnetic diffusion of the model is stronger than in the real plasma. Nevertheless, the effects of the reconnection region on the depletion of the magnetosheath and the injection of plasma into the inner magnetosphere are correctly reproduced to a first approximation. Finally, we note that we do not include the planet rotation and orbital motion in the current model yet either, and we leave this for future work.

The magnetosphere response to the stellar wind and the IMF shows several interlinked phases that must be distinguished. First, the response of the dayside magnetopause and magnetosheath can affect the magnetosphere standoff distance, the plasma flows toward the inner magnetosphere, and/or the location of the reconnection regions, among other things. Next, the response of the magnetotail, which is followed by the ionospheric response and, subsequently, by the ring current response. In this paper, our analysis is mainly focused on the dayside response of the magnetosphere; we also discuss some implications regarding the magnetic field at the nightside, although we do not aim at a detailed analysis of the magnetotail. Finally, the response of the ionosphere and ring current are beyond the scope of the present study.

We assume that a simulation is completed when it reaches a steady state. Therefore, we do not include dynamic events caused by the evolving space weather conditions (we do not modify the stellar wind and IMF parameters along the simulation). Typically, a simulation reached steady state after $\tau = L/V = 15$ code times, equivalent to $t \approx 16$ min of physical time, although the magnetosphere topology on Proxima b dayside is steady after $t \approx 11$ min, or about 10 code times. Consequently, the code can accurately reproduce the magnetosphere response if space weather conditions are roughly steady for time periods of $t = 10$–15 min.

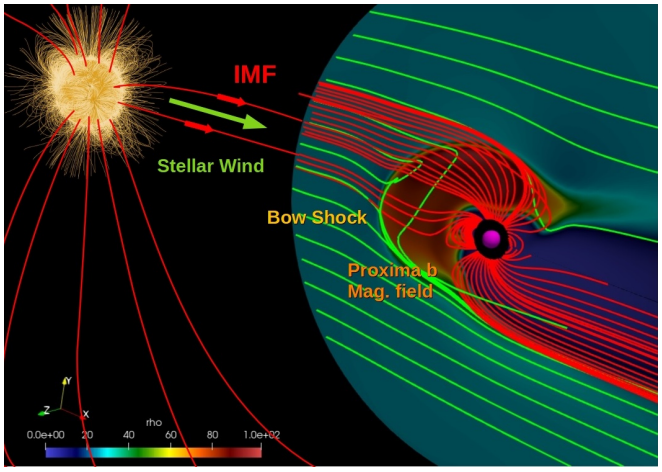

Fig. 1. Sketch of the magnetospheric interaction in the star-planet system Proxima–Proxima b. The stellar wind velocity and the interplanetary magnetic field (IMF) streamlines (assumed to be radial; see text in Sect. 3) are drawn in green and red, respectively. There are magnetic field lines from the star (yellow circle) that are connected to the exoplanet Proxima b (purple circle). The density distribution is shown as a color scale, normalized to the value of the stellar wind density, $\rho_{sw} = \mu m_p n_{sw}$ (see Table 1). The sketch represents a super-Alfvénic case, where the ram pressure of the wind dominates over the stellar wind magnetic field pressure, so a bow shock is formed at the dayside of the planet. The Proxima star is beyond the limits of our simulation domain.

3. Proxima b as a case study

Previous 3D MHD studies of the space weather of Proxima b showed that the planet may be subject to stellar wind pressures of up to three orders of magnitude higher than those experience by the Earth from the solar wind (e.g., Garraffo et al. 2016). Those authors found that Proxima is also subject to pressure changes of 1−3 orders of magnitudes within a day, dramatically altering the magnetopause standoff distance of the planet by factors of 2 to 5. Garraffo et al. (2016) also found that Proxima b likely passes in and out for the Alfvén surface, thus exposing the planet to both subsonic and supersonic wind conditions. More recent MHD simulations of the space weather of Proxima b by Garraffo et al. (2022) confirmed the finds described above, and showed that the large-scale magnetic field of the star does play a very significant influence on the ambient stellar wind, while the small-scale field does not. Kavanagh et al. (2021) also carried out MHD simulations of Proxima Cen, using an Alfvén wave-driven stellar wind model. They found that the mass loss rate of Proxima Cen stellar wind was $\dot{M}_\star \simeq 0.25\ \dot{M}_\odot$, corresponding to $n_{sw} \sim 600$ cm^{-3}. For comparison, the simulations carried out by Garraffo et al. (2016) imply $\dot{M}_\star \simeq 0.75\ \dot{M}_\odot$ ($n_{sw} \sim 1800$ cm^{-3}). Kavanagh et al. (2021) found, contrary to Garraffo et al. (2016), that the orbit of Proxima b always lay beyond the Alfvén surface. In this case, there is no sub-Alfvénic star-planet interaction, and therefore no radio emission from such (sub-Alfvénic) interaction is expected to arise.

Here, we applied the 3D MHD PLUTO code with two main goals. First, to study and discuss the habitability of Proxima b, focusing on the effects of the intensity of the planetary magnetic field, B_p, and its inclination, i. As a direct estimator of planet habitability, we determined for each simulation run the standoff magnetopause distance, R_{mp}. Our second main goal is to determine the expected radio emission arising from the dissipated

Table 1. Main parameters of the PLUTO simulations.

Parameter	Calm space weather Sub-Alfvénic scenario	Calm space weather Super-Alfvénic scenario	Extreme space weather CME scenario
n_{sw} (cm^{-3})	50	50	250
$\|v_{sw}\|$ (10^7 cm s^{-1})	5	10	25
B_{IMF} (mG)	3.2	1.6	16
$B_{Proxima}$ (G)	1200	600	600
$B_{Proxima\,b}$ (G)	0.16–1.28	0.16–1.28	0.16–0.64
i	(0°–90°)	(0°–90°)	(0°–45°)

power at the reconnection sites on the magnetosphere, which we directly measured from our simulations. This is relevant for prospects of using radio observations to detect exoplanets and, even more important, to directly measure their respective magnetic fields.

Our simulations considered both calm and extreme (i.e., CME-like space weather conditions; see Table 1). In turn, for calm space weather conditions, we run simulations for two broadly different scenarios: (1) the planet is in the sub-Alfvénic regime, where the stellar wind magnetic pressure dominates over the wind's ram pressure; and (2) the planet is in the super-Alfvénic regime, where the ram pressure of the wind is larger than the magnetic pressure and a bow shock is formed. The distinction between the sub- and super-Alfvénic regimes can be easily parameterized by the Alfvén Mach number, $M_A = v_{sw}/v_A$, where v_{sw} is the speed of the plasma relative to the planetary body, and v_A is the Alfvén speed. $M_A < 1$ corresponds to the sub-Alfvénic regime, while $M_A > 1$ corresponds to the super-Alfvénic one. The IMF is purely radial in the model, and assumes an intense stretching effect of the stellar wind on the magnetic field lines of Proxima. This leads to a dominant radial component of the IMF at the orbital distance of Proxima b.

We show in Table 1 the values for the most relevant parameters of our PLUTO simulations and, for comparison, in Table 2 we show the parameters used in the MHD simulations by Garraffo et al. (2016) and Kavanagh et al. (2021).

We note that none of those works discuss the radio emission generated in the magnetosphere of Proxima b, which is one of the main goals of the present study.

The stellar wind density values, n_{sw}, in our simulations were 50–250 times larger than in the solar wind around the Earth, and correspond to mass-loss rates of the stellar wind, $\dot{M}_\star$, of $\simeq$0.02 $\dot{M}_\odot$ and $\simeq$0.1 $\dot{M}_\odot$ for the calm and CME-like scenarios, respectively. Those values are in agreement with the upper limit for the stellar wind of Proxima Cen of 0.2 $\dot{M}_\odot$ from astrospheric absorption measurements, found by Wood et al. (2001).

In the sub-Alfvénic case, we used a value of 3.2 mG for B_{IMF}which corresponds to the extrapolation of the Proxima Cen magnetic field at the pole (1200 G) at the orbital distance of Proxima. In the super-Alfvénic case, we set a value of B_{IMF} half as large as in the sub-Alfvénic scenario. However, we note that the magnetic field value of Proxima could be lower (e.g., Klein et al. 2021). Still, the values of Proxima Cen magnetic field considered here are consistent with previous works. Indeed, Reiners & Basri (2008) found a value of 600 ± 150 G for the average surface magnetic field. Also, 3D MHD simulations by Yadav et al. (2016) indicate that Proxima Cen undergoes strong variations of its magnetic field surface intensity during its ∼7-yr long cycle, starting from about 500 G and going up to 2000 G.

Table 2. Parameters in other 3D MHD simulations.

Parameter	Garraffo+2016	Kavanagh+2021
$\dot{M}_\star(\dot{M}_\odot)$	0.75	0.25
n_{sw} (cm^{-3})	1800	600
$\|v_{sw}\|$ (10^7 cm s^{-1})	13, 16	3–12
$B_{Proxima}$ (G)	600, 1200	200
$B_{Proxima\,b}$ (G)	0.1, 0.3	Unmagnetized
i	10°, 60°	0°

For the CME-like scenario, we set values of the stellar wind density and speed, and of B_{IMF} 5, 2.5 and 10 times larger than in the standard Super-Alfvénic scenario.

In our simulations, and without any loss of generality, we fixed the stellar wind temperature to $T_{sw} = 3 \times 10^5$ K and the planet surface temperature $T_{planet} = 1000$ K. We also note that we assume a dipolar magnetic field for the exoplanet.

For each sub- and super-Alfvénic case, we used the following values of the intrinsic planetary magnetic field: 0.16, 0.32, 0.64 and 1.28 G, with the value of 0.32 G being the nominal average magnetic field for the Earth. For the study of the effect of the tilt, we fixed the magnetic field to be $B_p = 0.32$ G (i.e., an Earth-like magnetic field) and used the following tilt values: $i \in$ [0, 7, 15, 23.5, 30, 45, 60, 75, 83, 90] deg. A value of $i = 0$ deg corresponds to the case when B_p is perpendicular to B_{IMF}, and $i = 90$ deg corresponds to the case when B_p is anti-aligned with respect to B_{IMF}. For the computation of the radio emission in Sect. 5, we fixed the efficiency factor in converting Poynting flux to radio emission to a value of $\beta = 2 \cdot 10^{-3}$ (Zarka 2007; Zarka et al. 2018).

In Fig. 2, we show the final, steady situations of two representative cases of our simulations. The top panel corresponds to a sub-Alfvénic scenario ($M_A < 1$). In this case, the bow shock around the exoplanet (the region with the highest density, in red) dissipates all the way throughout the simulation and, in practice, is never formed. We can still see some features reminiscent of a dying bow shock and, but those would have disappeared completely if we had extended the simulations for a longer time. The resulting radio emission originates therefore only from the reconnecting region of the exoplanet magnetosphere. The bottom panel illustrates a super-Alfvén case, when a bow shock is formed. The accelerated electrons producing the radio emission originate both from the reconnecting region of the exoplanet magnetosphere and from the bow shock.

In Fig. 3, we show close-up images of the region close to the planet, for the steady situation obtained from simulations under calm space weather conditions (top and middle panels),

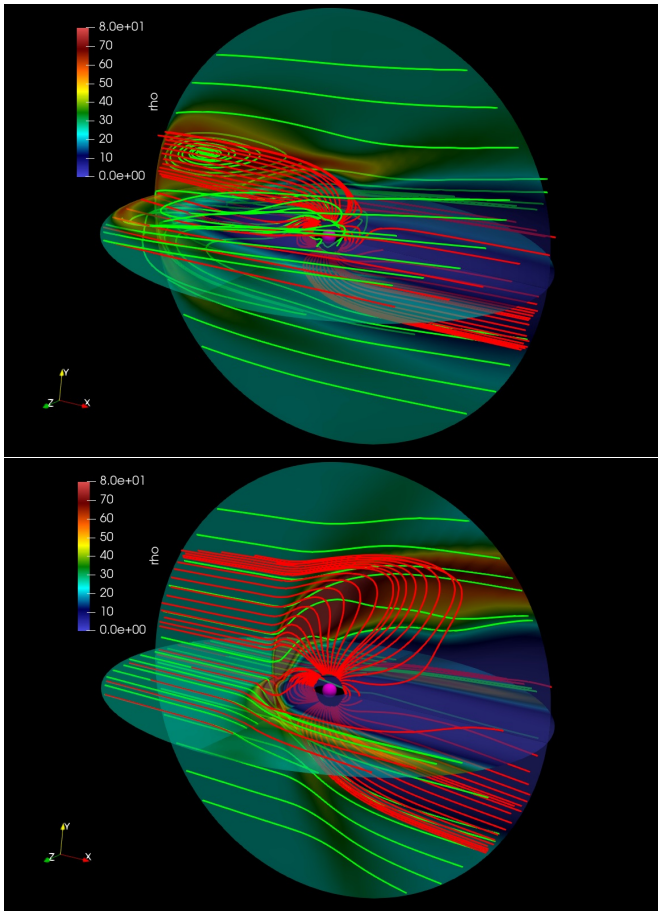

Fig. 2. Plots of density distribution (color scale, in particles cm^{-3}) for sub-Alfvénic (top) and super-Alfvénic (bottom) cases of our PLUTO simulations. The green lines correspond to streamlines of the stellar wind velocity, and the red lines to magnetic field lines of the stellar wind and of the planet. In both cases, B_p = 0.32 G and the tilt of the planet is i = 0 deg, i.e., B_p is perpendicular to B_{imf}. In the sub-Alfvénic case, no bow shock is formed, and the resulting radio emission originates only from the reconnecting region of the exoplanet magnetosphere. In the super-Alfvénic case, a bow shock is formed. The radio emission originates both from the reconnecting region of the magnetosphere and from the bow shock (see Sect. 5). Movies of these simulations, from beginning to end, when a steady solution is reached, are available online.

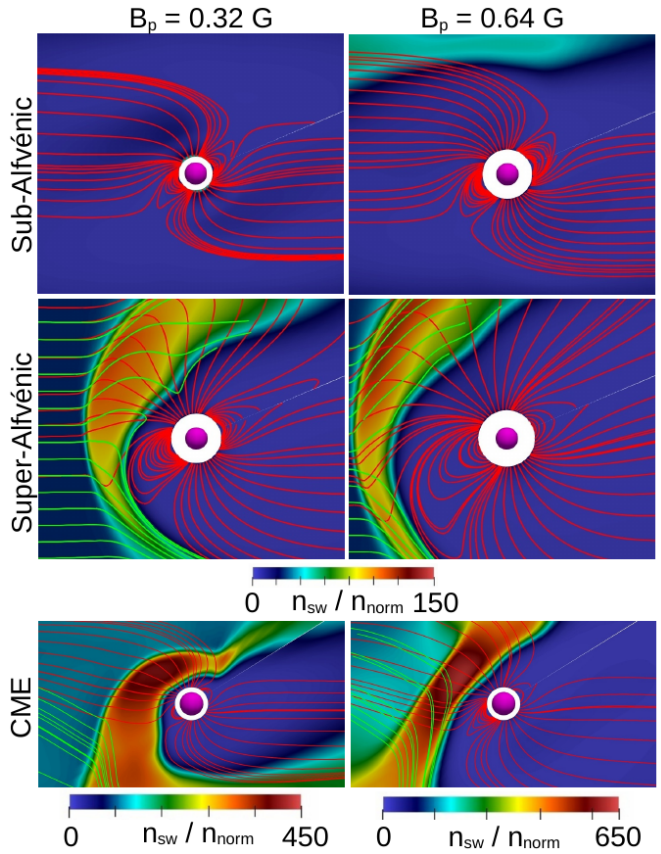

Fig. 3. Plots of density distribution (color scale, in particles cm^{-3}) for simulations under calm space weather conditions (top and middle panels), and under a CME (bottom panels), for two different magnetic field intensity values of the exoplanet Proxima b. The green and red lines are as described in Fig. 2.

and under extreme space weather (bottom panels), for two different values of the intensity of the magnetic field of Proxima b, B_p= 0.32 G and B_p= 0.64 G. As shown in Fig. 2, when the conditions are sub-Alfvénic, no bow shock is formed, while the bow shock can be clearly seen in the rest super-Alfvénic regime. We also note that as the exoplanetary magnetic field increases, the bow shock is formed farther away and the magnetopause standoff distance is larger, thus increasing the protection of the planet against damaging particle and radiation from outside (see Sect. 4 for a detailed discussion). We also note how the particle density is much larger in the bow shock region formed under extreme weather conditions (bottom panels), compared to that formed under calm space weather.

4. Proxima b habitability – magnetopause standoff distance

In this section, we determine the values of the magnetopause standoff distance, R_{mp}, in our simulations, both as a function of the tilt angle of Proxima b and of its magnetic field. We use R_{mp} to infer the habitability of Proxima b. Namely, if $R_{mp} \leq R_p$, then there is direct precipitation of damaging particles, and the habitability is strongly constrained. We note, however, that for the simulations under extreme weather conditions we set up a minimum value of $R_{in} = 1.5\,R_p$ since for smaller values there were numerical issues with the boundary conditions of the internal region. Therefore, for the CME simulations, if $R_{mp} \leq 1.5\,R_p$, we considered that there was direct particle precipitation on the exoplanet.

In the analysis of our simulations, we define R_{mp} as the radial distance to the last closed magnetic field line on the exoplanet dayside (similar to the case of Ganymede; see, e.g., Kivelson et al. 2004), at 0° longitude in the ecliptic plane (see Fig. 4). We therefore directly measured R_{mp} from our simulations, instead of using the (theoretical) magnetopause standoff distance, R_{mp}, which can be obtained from the balance between the pressures of the stellar wind and that of the exoplanet magnetosphere. The pressure of the stellar wind includes the dynamic, thermal and magnetic pressure components; the pressure of the exoplanet magnetosphere includes the thermal and (dipolar) magnetic field pressure. From that pressure balance, one gets R_{mp}/R_p (e.g., Varela et al. 2022b)

$$\frac{R_{mp}}{R_p} = \left[\frac{\alpha \mathcal{M}_p{}^2/\pi}{m_p n_{sw} v_{sw}^2 + \frac{B_{IMF}^2}{4\pi} + \frac{2 m_p n_{sw} c_{sw}^2}{\gamma} - m_p n_{bs} v_{th,msp}^2} \right]^{1/6}, \quad (5)$$

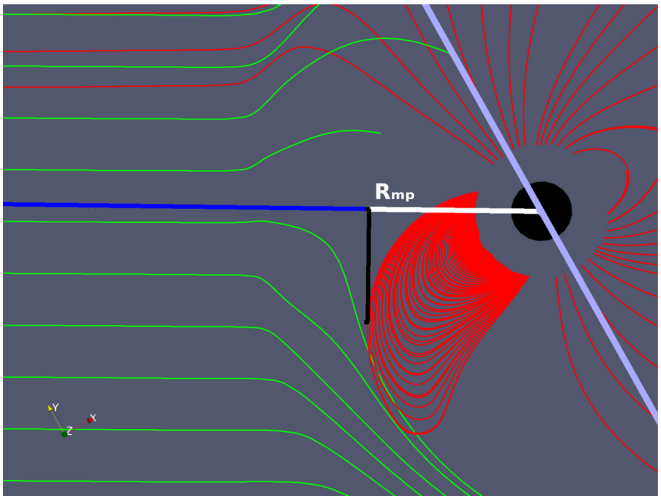

Fig. 4. Illustration of the measurement of the magnetopause standoff distance in our simulations. The black circle corresponds to the planet. The standoff distance is the radial distance (white line) to the projection of the last closed magnetic field of the planet (in red) on the line connecting the star and the planet (in blue). The simulation depicted here corresponds to a super-Alfvénic case, where the inclination of the magnetic axis of the planet with respect to the ecliptic is 30° (purple line) and B_p = 0.32 G.

where $\mathcal{M}_p$ is the exoplanet dipole magnetic field moment, α the dipole compression coefficient ($\alpha \approx 2$, Gombosi 1994), n_{bs} the particle number density in the bow shock, and $v_{th,msp}$ the speed of the thermal electrons in the magnetosphere, and the above expression is in cgs units. If $R_{mp}/R_p \leq 1$, then there is direct precipitation of the stellar wind plasma particles toward the exoplanet surface, and habitability is not possible.

We note that Eq. (5) is just an approximation, and the actual value of R_{mp} can depart significantly from the true value, as the above expression does not take into account a number of important effects. First, there is no topological consideration at all, and all terms in the equation are treated as simple scalar values. Second, this expression does not include the effect of the reconnections between the IMF with the exoplanetary magnetic field lines. Therefore, Eq. (5) assumes a compressed dipolar magnetic field, while ignores the orientation of the IMF. Third, Eq. (5) is only valid if the reconnection between the IMF and Proxima b magnetic field is rather weak.

As a consequence, the application of Eq. (5) to calculate the magnetopause standoff distance may depart signficantly with respect to the values determined from 3D MHD simulations, such as the ones we carry out in this work. In Fig. 5, we show the dependence of the normalized magnetopause standoff distance, $r = R_{mp}/R_p$, with the planet tilt (left panels) and with the magnetic field of Proxima b (right panels), for calm weather (both sub-Alfvénic and super-Alfvénic; top and middle panels, respectively) and extreme weather conditions (bottom panels), as described in Table 1. We note that, for any given set of values of n_{sw}, v_{sw}, B_{IMF} and B_p, Eq. (5) predicts a single value, whereas our simulations indicate values that range from $R_{mp} \approx R_p$ up to $R_{mp} \gtrsim 7\,R_p$, which clearly illustrates the point that the standard usage of Eq. (5) may lead to wrong results.

4.1. Calm space weather scenario

In this subsection, we discuss the results obtained for the sub-Alfvénic and super-Alfvénic simulations under calm space weather conditions. For the simulation runs as a function of the tilt of the planet, we used B_p = 0.32 G (i.e., an Earth-like magnetic field). First, we note that R_{mp} monotonically decreases with the tilt angle, independently of the Alfvénic regime of the planet. For a wide range of tilt values, R_{mp} is several times the planet radius, which means that the magnetic shield is enough to counteract the damaging cosmic radiation. For very large tilt angles, however, R_{mp} can be essentially equal to the planetary radius, which means that any damaging radiation goes unimpeded to the surface of the planet, and habitability will be severely threatened.

It should be noted that the magnetopause standoff distance is smaller in the sub-Alfvénic case, compared to the super-Alfvénic one. This result may seem counter-intuitive at first, since the dynamic pressure of the stellar wind is four times larger in the super-Alfvenic configuration, as the stellar wind velocity is twice as large (see Table 1). On the other hand, the magnetic pressure of the IMF is four times larger, so the reconnection intensity is stronger in the sub-Alfvenic case (since the IMF intensity is twice as large). This leads to an enhanced erosion of the magnetic field of Proxima b. Our simulations therefore imply that in the sub-Alfvénic case the effect of the IMF erosion on the magnetic field of Proxima is stronger than the effect of the enhanced magnetosphere compression in the super-Alfvenic case. We also recall that the pressure balance in the sub-Alfvénic case is different from that in the super-Alfvénic case because the effect of the thermal pressure of the bow shock disappears. Therefore, a direct comparison of the magnetopause standoff distance in both configurations can be misleading, since the entire pressure balance is different.

In our study of the dependence of R_{mp} on the Proxima b surface magnetic field, we used two different values of the tilt angle, 0° and 23.5°, the latter representing an Earth-like case. We note that, as expected, the larger the planetary magnetic field, the larger the value of R_{mp}, regardless of the Alfvénic regime. More specifically, R_{mp} nearly doubles when B_p increases from 0.16 to 1.28 G: from 4.7 R_p to 9.0 R_p for the sub-Alfvénic regime, and from 6.9 R_p to 12.6 R_p in the super-Alfvénic regime for planet with no inclination. For a planet with an inclination of 23.5°, as in the case of the Earth, R_{mp} increases from 3.6 R_p to 7.2 R_p in the sub-Alfvénic regime, and from 5.6 R_p to 10.2 R_p in the super-Alfvénic regime. This trend agrees with the expected behavior for R_{mp} from Eq. (5). Indeed, since $R_{mp} \propto \mathcal{M}_p{}^{1/3}$, and given that $\mathcal{M}_p \propto B_p$, it follows that $R_{mp} \propto B_p^{1/3}$. Since we used values from 0.16 G up to 1.28 G, the theoretical value of R_{mp} increases by a factor of $8^{1/3} = 2$, which is almost exactly the increase shown by R_{mp} in the right panels of Fig. 5. The main conclusion from those simulations is that if the magnetic field of Proxima b is Earth-like or larger, it suffices to counteract the role of the total pressure of the stellar wind.

On the other hand, the behavior of R_{mp} as a function of the tilt angle cannot be recovered from Eq. (5). Our simulations clearly show that as the planetary tilt increases, the magnetopause standoff distance decreases, leading eventually to values that constrain the habitability of Proxima b.

We also note that for our sub-Alfvénic simulations we considered that the stellar wind speed was half the one we used for the super-Alfvénic cases, and the interplanetary magnetic field was twice as large, significantly enhancing the effect of the magnetic reconnection between the planetary and interplanetary magnetic fields. In the sub-Alfvénic case magnetic erosion is therefore quite dominant, which greatly shrinks the magnetopause. In both cases, the standoff distance is large enough that there would be no stellar wind precipitation on the planet, at least

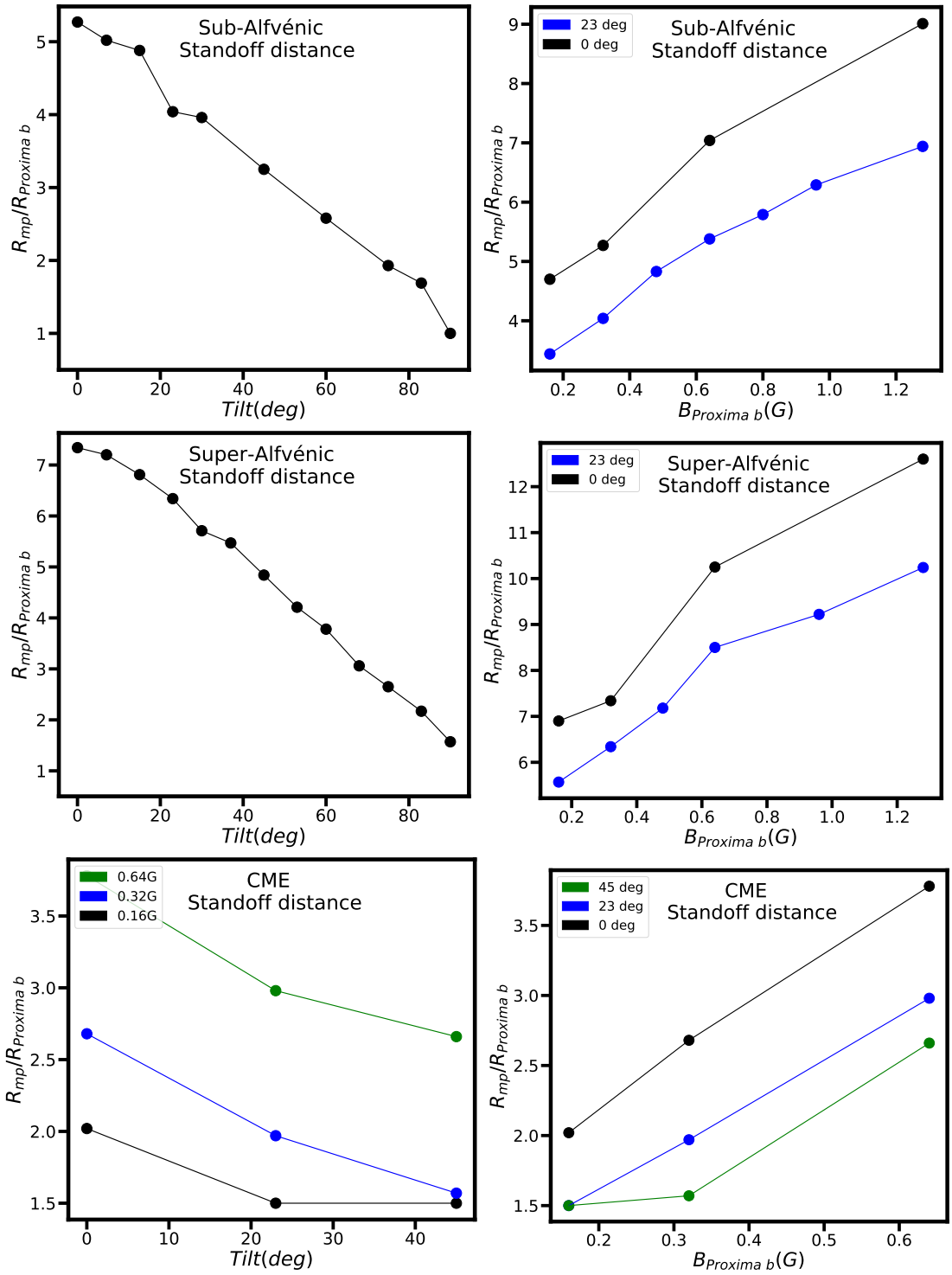

Fig. 5. Magnetopause standoff distance as a function of the tilt of the planet (left panels) and of the intrinsic planetary magnetic field, B_p (right panels). The top and middle panels correspond to the sub-Alfvénic and super-Alfvénic cases, respectively, while the bottom panels correspond to a CME-like scenario. The top and middle left panels were obtained for a value of $B_p = 0.32$ G.

during regular space conditions. The exception is the case with a very high planet tilt (close to 90°), when the standoff distance decreases to values of 1 and 1.57 R_p for the sub- and super-Alfvénic cases, respectively, which would make habitability not possible in the sub-Alfvénic case, as there would be direct precipitation of stellar wind particles, and in the super-Alfvénic case would be extremely vulnerable to even relatively small variations in the activity of the host star.

4.2. CME scenario

The bottom panels of Fig. 5 show the results of PLUTO simulations for extreme space weather conditions around Proxima b, such as those produced by a CME from its host star. We recall that in those simulations we had to set up a minimum value of 1.5 R_p for the inner boundary radius of the planet, which effectively means that if the value of R_{mp} drops down to 1.5 R_p,

there is direct precipitation of particles onto the planet. Since the dynamic and magnetic pressure of the wind are so large, the magnetopause standoff distance is significantly smaller with respect to either the sub-Alfvénic or super-Alfvénic cases, as a function of either the tilt angle, i, or of B_p. The bottom left panel shows, as expected, that the larger the tilt, the smaller the value of R_{mp}. In fact, for tilts above ∼45°, all simulations yielded values of $R_{mp} \lesssim 1.5\,R_p$, implying that there is direct particle precipitation onto the planet. If the planet has a small tilt, even a relatively small value of B_p is enough to shield the planet. However, if the tilt is similar to that of the Earth or larger, B_p also needs to be similar to or higher than that of our planet to permit magnetic shielding.

5. Radio emission from Proxima b

The detection of radio emission from the magnetosphere of an exoplanet is probably the only direct way of determining its magnetic field. This is of huge relevance for the understanding of the interiors of exoplanets. Once the characteristics of the exoplanet magnetic field are inferred, it becomes feasible to study the space weather conditions generated by the host star on the exoplanet orbit. Therefore, the radio emission from the exoplanet magnetosphere and the space weather conditions to which the exoplanet is subject are tightly intertwined. In addition, radio emission estimates from numerical modeling are useful to guide future observations of star-planet systems, aimed at the detection of new worlds using radio interferometers. In this section, we present estimates of the radio emission expected to arise from the magnetospheric reconnection regions, both under calm and extreme space weather conditions around Proxima b. The predicted radio emitted power from the interaction between the stellar wind of Proxima and the magnetosphere of its planet Proxima b is therefore one of the main results from our numerical modeling.

We followed the radio-magnetic Bode's law, and used the incident magnetized flow power and the obstacle magnetic field intensity to determine the radio emission as $P_R = \beta P_B$, where β is the efficiency of converting the dissipated power, P_B, into radio emission power, and $\beta \approx (2\text{–}10) \times 10^{-3}$ (Zarka 2018). We calculated the power dissipated in the interaction between the stellar wind and the magnetosphere at the exoplanet dayside. Irreversible processes in the interaction convert internal, bulk flow kinetic and magnetic energy into the kinetic energy required to accelerate the electrons along the magnetic field lines, leading to cyclotron-maser radiation emission by these accelerated electrons (see Varela et al. 2022b for details.) The radio emission, using the net magnetic power deposited on the exoplanet day side, is therefore

$$P_R = \beta P_B = \beta \int_V \boldsymbol{\nabla} \cdot \frac{(\mathbf{v} \wedge \boldsymbol{B}) \wedge \boldsymbol{B}}{4\pi} \mathrm{d}V, \tag{6}$$

where P_B is the divergence of the magnetic Poynting flux associated with the hot spots of energy transfer in the exoplanet day side, and V is the volume enclosed between the nose of the bow shock and the magnetopause. We note that we directly measure the radio emission, analyzing our numerical results (see Appendix B), not by applying any approximate formula, other than the empirical factor β, as often done in the literature.

We note that the accelerated electrons that travel along the magnetic field lines generate cyclotron-maser emission near Proxima b (planetary emission) or close to the star (we call this emission from star-planet interaction). The latter emission is expected to be produced only in the sub-Alfvénic regime, since one of the Alfvén wings is able to efficiently carry momentum and energy back to the star. In contrast, planetary emission can be produced both in the sub- and super-Alfvénic regimes, since the radio-magnetic scaling law may hold in both cases. Our current analysis is focused on the emission from particles coming from the magnetopause reconnection regions, in particular the Poynting flux originated on the dayside, which likely dominates the overall radio emission budget, and therefore is enough to estimate the radio emission power, independently of the precise details of physical processes happening in the magnetosphere that lead to radio emission (e.g., Dungey cycle and electron acceleration). Figure 6 summarizes our results for both calm space weather and extreme space weather conditions. In that figure, we show the radio emitter power, P_R, as a function of planet tilt (left panels) and of the magnetic field of Proxima b (right panels).

5.1. Radio emission under calm space weather conditions

The radio emission in the sub-Alfvénic scenario is produced only by charged particles coming from the magnetopause reconnection regions between the interplanetary magnetic field and the exoplanet magnetic field, as no bow shock is formed. In the super-Alfvénic scenario, there is contribution from both the particles from the magnetopause and the bow shock, which is linked to the interplanetary magnetic field pile-up and bending. We therefore obtained the individual contributions of particles coming from the magnetopause and the bow shock to facilitate comparisons, we summarize our results in Fig. 6.

The top panels of Fig. 6 correspond to the analysis from the simulations for the sub-Alfvénic regime (see Table 1 of Proxima b. Since no bow shock is formed, the dissipated power (and accelerated electrons) comes only from the magnetopause region. The top left panel shows the radio emission as a function of the planetary tilt. The radio emission decreases slightly, from the case with no tilt to values of about 20°. For larger tilts, the radio emission monotonically increases, reaching approximately $2{\times}10^{19}$ erg s^{-1}, which are about two to three times larger than for medium tilt values.

The decrease of the radio emission in the cases with low tilt values is due to a weakening of the reconnection between the IMF and the magnetic field of Proxima b in the southern region of the magnetopause. As the tilt value increases, the reconnection region moves from the southern to the equatorial region of Proxima b, which enhances the reconnection and leads to larger radio emission. The value of the radio emission reaches a maximum when the field lines of B_{IMF} and of B_p are parallel in the nose of the bow shock region (i.e., for a tilt of 90°).

The radio emission also increases steadily as a function of the exoplanetary magnetic field (top right panel), as expected from Eq. (6), reaching a maximum value for B_p = 1.28 G of $\sim 2.2 \times 10^{19}$ erg s^{-1}. The increment of the radio emission with the magnetic field intensity of Proxima b is linked to the generation of a wider reconnection region, located farther away from the exoplanet surface, as shown in the bottom panels of Fig. 7. We also note how similar the behavior of the radio emission is versus exoplanetary magnetic field for the cases with $i = 0°$ and $i = 23.5°$ (top panels of Fig. 7). This is due to the generation of wider reconnection regions as the magnetic field of Proxima b increases, which reduces the impact of small variations of the tilt on the radio emission as the magnetic field of Proxima is stronger.

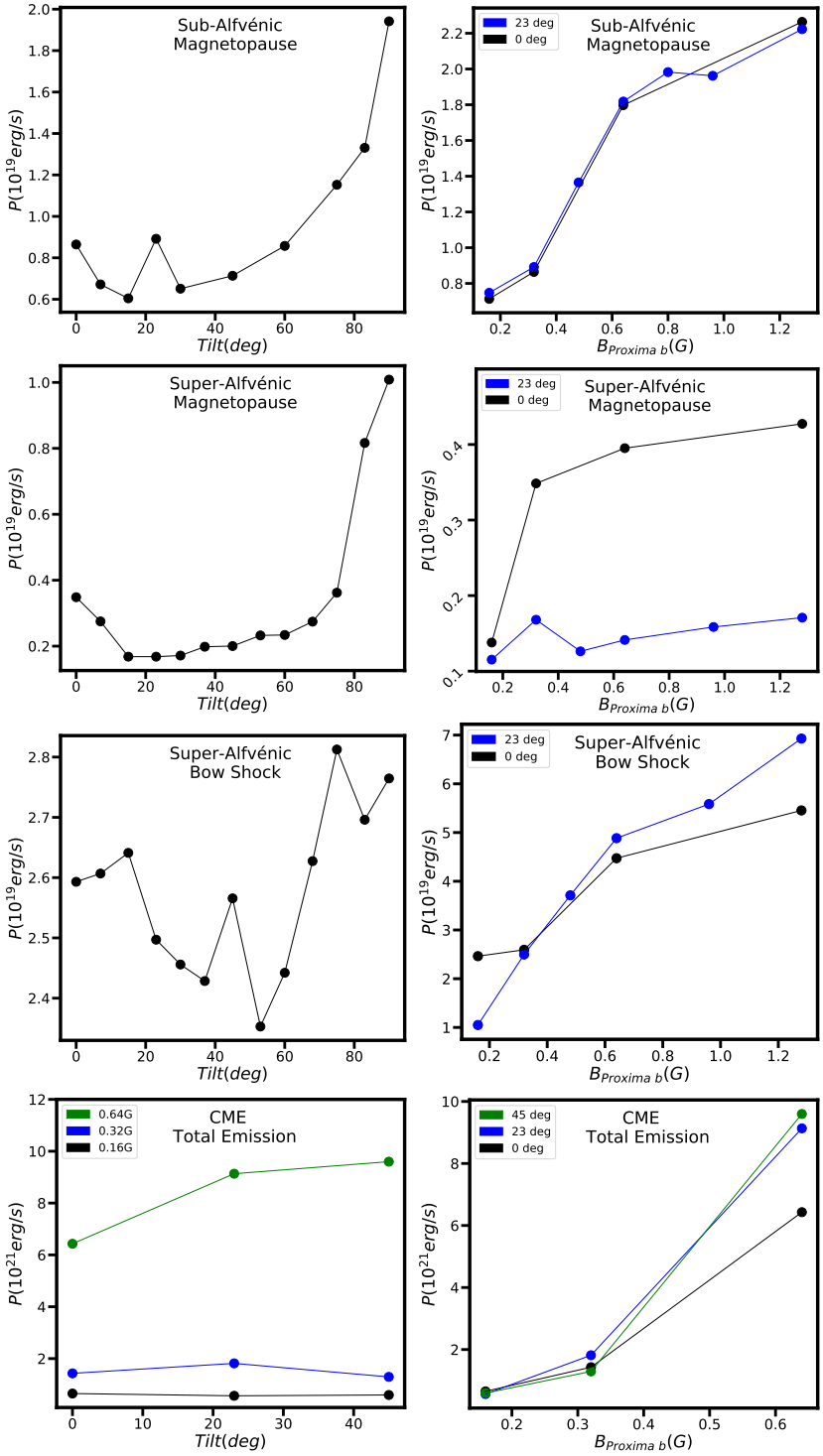

Fig. 6. Radio emission from the interaction of the stellar wind and the planetary magnetosphere of Proxima b for calm space weather conditions (sub-Alfvénic case, top panels; super-Alfvénic case, upper and lower middle panels) and extreme weather conditions (CME-like case, bottom panels), as a function of the tilt angle and of the magnetic field of Proxima b. The top and upper middle panels correspond to the contribution from the magnetopause region, while the lower middle panels correspond to the contribution from the bow shock in the super-Alfvénic scenario. For the CME-like case, the contribution is the total (magnetopause + bow shock).

We show in the upper and lower middle panels of Fig. 6 the expected radio emission in the super-Alfvénic regime, as a function of the planetary tilt (left panels), where we set a value of B_p = 0.32 G (Earth-like value) for all runs, and as a function of the planetary magnetic field (right panels). In this case, both a magnetopause and a bow shock are formed, and those cases are shown in the upper and lower middle panels, respectively. The overall trend of the radio emission from the magnetopause as a function of the tilt angle (middle left panels) is similar to the sub-Alfvénic case, although the emitted power is at most of $\simeq 10^{19}$ erg s^{-1}, about a factor of two smaller than that produced in the sub-Alfvénic case. The radio emission in the super-Alfvénic

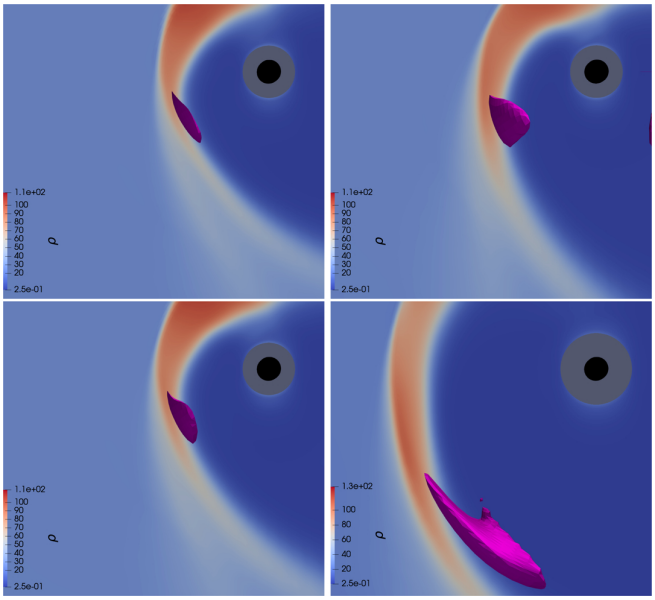

Fig. 7. Close-up images of the region of interaction of the interplanetary magnetic field and that of Proxima b. The top panels highlight the effect of the tilt angle (15° and 37° for the left and right panels, respectively, for a fixed value of B_p = 0.32 G. The bottom panels show the effect of the planetary magnetic field on the reconnection region (0.32 G and 1.28 G for the left and right panels, for a fixed tilt of 23.5°). The interaction region is clearly farther away from the planet for the case of B_p = 1.28 G. The reconnection region (in pink) is defined as the region where the local magnetic field is ≤0.32 mG, corresponding to seven times the normalized magnetic field value in our simulations. The planet Proxima b is shown as a black circle.

cases is smaller because the IMF intensity is half compared to the sub-Alfvénic case (Table 1) and the pile-up of the IMF lines is larger due to the presence of the bow shock.

The radio emission of the magnetopause as a function of the Proxima b magnetic field (upper middle right panel) increases with the magnetic field, by almost a factor of three between the cases with B_p = 0.16 and B_p = 1.28 G, which is a factor similar to that seen in the sub-Alfvénic cases. We also note that the radio emission is systematically smaller for a tilt equal to that of the Earth, with respect to $i = 0°$, in agreement with the result seen in the upper middle left panel. The radio emission from the bow shock as a function of the tilt angle does not show any evident trend. It appears that the emitted power is, within the uncertainties of the simulations, consistent with being constant, at a level of about $\sim 2.6 \times 10^{19}$ erg s^{-1}, suggesting that the planetary tilt plays a minor role, or no role at all, in the contribution of the bow shock to the radio emission. Finally, the radio emission from the bow shock as a function of B_p (lower middle right panel) indicates that it monotonically increases with B_p reaching values of up to 7×10^{19} erg s^{-1}. The contribution from the bow shock is about an order of magnitude larger than that of the magnetopause, and is therefore the one that dominates the overall budget in the super-Alfvénic regime. Further, there does not seem to be a strong difference in the radio emission for the cases with $i = 0°$ and $i = 23.5°$, in agreement with the study of the radio emission as a function of i.

There seems to be a trend in the dissipated radio power as a function of the planetary magnetic field (see panels for the sub-Alfvénic – magnetopause and super-Alfvénic – bow shock cases in Fig. 6). We fitted our data to a power law $P_R = P_0 \times \left(B_p/1\mathrm{G}\right)^k$, where P_0 is the radio power for B_p = 1 G.

For the sub-Alfvénic magnetopause emission, we obtain $P_0 = (2.1 \pm 0.1) \times 10^{19}$ erg s^{-1} and $k = 0.7 \pm 0.1$. For the super-Alfvénic bow shock emission, $P_0 = (5.7 \pm 0.6) \times 10^{19}$ erg s^{-1} and $k = 0.7 \pm 0.1$. For the super-Alfvénic magnetopause emission the fit does not show any clear correlation between P_R and B_p.

5.2. Radio emission under CME-like conditions

The bottom panels of Fig. 6 show the predicted radio emission in a CME-like, super-Alfvénic scenario for Proxima b, as a function of the planetary tilt (left) and as a function of the planetary magnetic field (right). Unlike in the super-Alfvénic case under calm space weather conditions discussed in the previous subsection, here we do not separate the contribution of the magnetopause from that of the bow shock, and therefore give only the total contribution, which is anyway completely dominated by the bow shock. We note that the radio emission is more than two orders of magnitude larger than under calm weather conditions, whether in the sub-Alfvénic or super-Alfvénic regime. For a given magnetic field, there is no clear dependence with the tilt angle. On the other hand, the predicted radio emission as a function of the planetary magnetic field has an approximate B_p^2 dependence, as could be expected from Eq. (6).

The total radio power in the CME-like scenario shows also a correlation with the planetary magnetic field. As in the calm space weather scenario, we fit the data to a power-law and find that $P_0 = (1.7 \pm 0.3) \times 10^{22}$ erg s^{-1} and the index of the power-law is $k = 1.9 \pm 0.2$. This value is significantly higher than in the case of calm space weather conditions, and compatible with $P_R \propto B_p^2$.

We note that in the CME-like scenario, both the bow shock and the magnetopause are closer to the planet than in the calm space weather scenario. In particular, the dynamic pressure of the stellar wind in the CME-like scenario is 30 times higher, which leads to a much more compressed configuration of the magnetosphere. The asymmetry induced by the IMF on the magnetic field of Proxima b is much smaller in this case, as the magnetic field close to Proxima b is more intense, and dominates over that of the IMF, despite it being 10 times larger than in the calm space weather scenario (super-Alfvénic). Therefore, those results might suggest that when the effect of the IMF on the magnetic topology of Proxima b is small in the CME-like scenario, the standard behavior $P_R \propto B_p^2$ is recovered. If, on the other hand, the asymmetry induced by the IMF is large (calm space weather scenarios), then the dependence of P_R with B_p deviates from that standard behavior.

In summary, the total radio emitted power obtained in the simulations is in the range of $\sim(0.7–2) \times 10^{19}$ erg s^{-1} and $\sim(1.2–7.5) \times 10^{19}$ erg s^{-1} for the sub-Alfvénic and super-Alfvénic regimes, respectively, under calm space weather conditions. Those values correspond to radio flux densities in the range of 0.3–1.0 mJy and up to about 3 mJy, for the sub-Alfvénic and super-Alfvénic regimes, respectively, assuming an isotropic emission ($\Omega = 4\pi$) and that the emission bandwidth is of 0.9 MHz, which is the value corresponding to the electron-cyclotron frequency of a planetary magnetic field of 0.32 G. If Proxima b is subject to a more extreme space weather (e.g., a CME event), the predicted flux densities are more than about 100 times larger than when the planet is under calm average space weather conditions.

Pérez-Torres et al. (2021) measured radio emission values from the Proxima–Proxima b system from ∼200 μJy (steady emission) up to a few tens of mJy (bursty emission), using the

Australia Telescope Compact Array at a frequency of ~1.6 GHz. While the coherent radio emission detected by Pérez-Torres et al. (2021) spread across a band of about ~200 MHz and used a different efficiency factor in the conversion of the dissipated power to the radio power, those values broadly agree with the observations, which suggests that, if Proxima b is at times in a sub-Alfvénic regime, then radio emission from star-planet interaction can be detected. Not less important, our MHD simulations yield additional support to sub-Alfvénic interaction as a viable way for detecting signatures of exoplanets, although disentangling the emission from star-planet interaction from that of the star itself is challenging, and requests that the signal appears correlated with the orbital period of the (known) planet to confirm its star-planet interaction nature. In the super-Alfvénic scenario the planetary emission can reach a few mJy and, if the planet is subject to a CME event, up to a few hundred mJy. Although those values are huge, the emission frequency falls, even in its second harmonic, well below the cutoff frequency of the Earth ionosphere, and therefore cannot be detected from Earth if the magnetic field of Proxima b is similar to the one of our planet.

6. Summary

In this paper, we discussed the habitability of Proxima b, as well as the expected radio emission that arises from the interaction of the stellar wind magnetic field with that of the planet, by characterizing the magneto-plasma environment of Proxima b when the planet is subject to either calm average space weather conditions or subject to more extreme CME-like conditions. We studied the role of the stellar wind and planetary magnetic field, and their mutual orientation, using the 3D MHD code PLUTO (Mignone et al. 2007), both for the sub-Alfvénic and super-Alfvénic regimes. We also predicted the radio emission generated from the interaction between the stellar wind of Proxima and the magnetosphere of its planet Proxima b, which is relevant to guide radio observations aimed at unveiling planets. Compared to previous MHD simulations of the space weather around Proxima b, we measure the magnetopause standoff distance of Proxima b, R_{mp}, directly from our simulations. This is unlike the simulations performed in other works where an approximate analytical expression is used, which can lead to values of R_{mp} that largely depart from the true values. Likewise, we determined from our simulations the expected radio emission from the exoplanet dayside magnetosphere reconnection regions around Proxima b, which is relevant not only for the predictions regarding Proxima b, but also for any Earth-like planet.

The main outcomes from this study are the following:

The magnetopause standoff distance, R_{mp}, decreases with the tilt, i, and increases with B_p (Fig. 5), both under calm and extreme space whether conditions. If Proxima b has a magnetic field similar to that of the Earth (B_p=0.32 G) or larger, the shielding provided by the planetary magnetopause under calm space weather conditions is more than enough for any planetary tilt angle, i, but the most extreme ones when i is close to 90°. Even if the magnetic field is lower than that of the Earth, the magnetopause provides sufficient shielding as long as the planetary tilt is similar to that of the Earth or smaller. If Proxima b is subject to more extreme space weather conditions (e.g., a CME event) from its host star, the planet is well shielded if the planet is an Earth-like planet (B_p= 0.32 G, i = 23.5°), has a smaller tilt, or has a larger planetary magnetic field.

We note that R_{mp} is smaller in the sub-Alfvénic case, compared to the value for the super-Alfvénic case. This paradoxical result appears because the dynamic pressure of the stellar wind is four times larger in the super-Alfvenic configurations. On the other hand, the magnetic pressure of the IMF is four times larger in the sub-Alfvénic case, so the reconnection intensity is stronger. This leads to an enhanced erosion of the magnetic field of Proxima b. Our simulations therefore imply that in the sub-Alfvénic case the effect of the IMF erosion on the magnetic field of Proxima is stronger than the effect of the enhanced magnetosphere compression in the super-Alfvénic case.

We also determined the radio emission generated from the interaction between the stellar wind of Proxima and the magnetosphere of Proxima b, which is relevant to guiding radio observations aimed at unveiling planets. We find that, under calm space weather conditions, the radio emission caused by the dayside reconnection regions can be as high as 7×10^{19} erg s^{-1} in the super-Alfvénic regime, and is on average almost an order of magnitude larger that the radio emission in the sub-Alfvénic case. This is due to the much larger contribution of the bow shock to the overall radio emission budget, which is not formed in the sub-Alfvénic regime. We also find that the emission from the bow shock has a rather weak dependence on the tilt angle of the planet. If Proxima b is subject to extreme space weather conditions, the radio emission is more than two orders of magnitude larger than under calm space weather conditions. For a given planetary magnetic field, there is no clear trend of the expected radio emission with the tilt angle. On the other hand, we find that $P_R \propto B_p^{1.9\pm0.1}$. This result might suggest the effect of the IMF on the magnetic topology of Proxima b is small in the CME-like scenario, leading to the standard scaling $P_R \propto B_p^2$, unlike in the calm space weather scenario, where the asymmetry induced by the IMF on the magnetic topology of the planet is large, which weakens the dependency of P_R on B_p.

The radio emission power from the interaction of the Proxima stellar wind with the magnetosphere of Proxima b should therefore result in flux densities at the distance of the Earth of up to a few mJy under calm space weather conditions (a few hundred mJy, if the planet is affected by CME-like events). However, the frequency of this radio emission falls below the ionosphere cutoff, and cannot therefore be detected from the Earth, but would require sensitive radio interferometric arrays beyond the ionosphere. On the other hand, this result yields expectations for a direct detection (from Earth) in radio of giant planets in close-in orbits, as these Jupiter-like planets are expected to have magnetic fields that are large enough that their electron-cyclotron frequency falls above the ionosphere cutoff.

Acknowledgements. L.P.M. and M.P.T. acknowledge financial support through the Severo Ochoa grant CEX2021-001131-S and the National grant PID2020-117404GB-C21, funded by MCIU/AEI/ 10.13039/501100011033. JVR acknowleges support through project 2019-T1/AMB-13648, funded by the Comunidad de Madrid. LPM also acknowledges funding through grant PRE2020-095421, funded by MCIU/AEI/10.13039/501100011033 and by FSE Investing in your future. We also acknowledge the Spanish Prototype of an SRC (SPSRC) service and support financed by the Spanish Ministry of Science, Innovation and Universities, by the Regional Government of Andalusia, by the European Regional Development Funds and by the European Union NextGenerationEU/PRTR. P.Z. acknowledges funding from the ERC under the European Union's Horizon 2020 research and innovation programme (grant agreement no. 101020459 – Exoradio).

References

Airapetian, V. S., Barnes, R., Cohen, O., et al. 2020, Int. J. Astrobiol., 19, 136
Anglada-Escudé, G., Amado, P. J., Barnes, J., et al. 2016, Nature, 536, 437
Barnes, R. 2017, Celest. Mech. Dyn. Astron., 129, 509
Büchner, J., Dum, C., & Scholer, M. 2003, Space Plasma Simulation (Springer-Verlag Berlin Heidelberg)
Bunescu, C., Vogt, J., Marghitu, O., & Blagau, A. 2019, Ann. Geophys., 37, 347

Cohen, O., Drake, J. J., Glocer, A., et al. 2014, ApJ, 790, 57
Dedner, A., Kemm, F., Kröner, D., et al. 2002, J. Comput. Phys., 175, 645
De Keyser, J., Dunlop, M., & Owen, C. 2005, Space Sci. Rev., 118, 231
Dungey, J. W. 1961, Phys. Rev. Lett., 6, 47
Garcia-Sage, K., Glocer, A., Drake, J. J., Gronoff, G., & Cohen, O. 2017, ApJ, 844, L13
Garraffo, C., Drake, J. J., & Cohen, O. 2016, ApJ, 833, L4
Garraffo, C., Alvarado-Gómez, J. D., Cohen, O., & Drake, J. J. 2022, ApJ, 941, L8
Gombosi, T. I. 1994, Gaskinetic Theory, (Cambridge University Press)
Grießmeier, J. M., Stadelmann, A., Penz, T., et al. 2004, A&A, 425, 753
Grießmeier, J. M., Stadelmann, A., Motschmann, U., et al. 2005, Astrobiology, 5, 587
Gronoff, G., Arras, P., Baraka, S., et al. 2020, J. Geophys. Res. (Space Phys.), 125, e27639
Hapgood, M. 2019, Space Weather, 17, 950
Hess, S. L. G., & Zarka, P. 2011, A&A, 531, A29
Hess, S., Mottez, F., Zarka, P., & Chust, T. 2008, J. Geophys. Res. (Space Phys.), 113, A03209
Jakosky, B. M., Grebowsky, J. M., Luhmann, J. G., & Brain, D. A. 2015, Geophys. Res. Lett., 42, 8791
Kaiser, M. L., & Desch, M. D. 1984, Rev. Geophys., 22, 373
Kavanagh, R. D., Vidotto, A. A., Klein, B., et al. 2021, MNRAS, 504, 1511
Khodachenko, M. L., Ribas, I., Lammer, H., et al. 2007, Astrobiology, 7, 167
Kilpua, E. K. J., Lugaz, N., Mays, M. L., & Temmer, M. 2019, Space Weather, 17, 498
Kivelson, M. G., Bagenal, F., Kurth, W. S., et al. 2004, in Jupiter. The Planet, Satellites and Magnetosphere, 1, eds. F. Bagenal, T. E. Dowling, & W. B. McKinnon, 513
Klein, B., Donati, J.-F., Hébrard, É. M., et al. 2021, MNRAS, 500, 1844
Lammer, H., Lichtenegger, H. I. M., Kulikov, Y. N., et al. 2007, Astrobiology, 7, 185
Low, B. C. 2001, J. Geophys. Res., 106, 25141
Mignone, A., Bodo, G., Massaglia, S., et al. 2007, ApJS, 170, 228
Mishra, R., Cemeljic, M., Varela, J., & Falanga, M. 2023, ApJ, 959, L13
Neugebauer, M., & Goldstein, R. 1997, Washington DC Am. Geophys. Union Geophys. Monogr. Ser., 99, 245
Pérez-Torres, M., Gómez, J. F., Ortiz, J. L., et al. 2021, A&A, 645, A77
Pineda, J. S., & Villadsen, J. 2023, Nat. Astron., 7, 569
Reiners, A., & Basri, G. 2008, A&A, 489, L45
Ribas, I., Bolmont, E., Selsis, F., et al. 2016, A&A, 596, A111
Ridley, A., De Zeeuw, D., Manchester, W., & Hansen, K. 2006, Adv. Space Res., 38, 263
Ritter, P., Luhr, H., & Rauberg, J. 2013, Earth Planets Space, 65, 1285
Samsonov, A. A., Gordeev, E., Tsyganenko, N. A., et al. 2016, J. Geophys. Res.: Space Phys., 121, 6493
Scalo, J., Kaltenegger, L., Segura, A. G., et al. 2007, Astrobiology, 7, 85
Shields, A. L., Ballard, S., & Johnson, J. A. 2016, Phys. Rep., 663, 1
Shume, E. B., de Paula, E. R., Maus, S., et al. 2009, J. Geophys. Res.: Space Phys., 114, A06305
Suárez Mascareño, A., Rebolo, R., & González Hernández, J. I. 2016, A&A, 595, A12
Suzuki, T. K. 2013, Astron. Nachr., 334, 81
Trigilio, C., Biswas, A., Leto, P., et al. 2023, ApJ, submitted [arXiv:2305.00809]
Turbet, M., Leconte, J., Selsis, F., et al. 2016, A&A, 596, A112
Turner, J. D., Zarka, P., Grießmeier, J.-M., et al. 2021, A&A, 645, A59
Varela, J., Pantellini, F., & Moncuquet, M. 2015, Planet. Space Sci., 119, 264
Varela, J., Pantellini, F., & Moncuquet, M. 2016a, Planet. Space Sci., 129, 74
Varela, J., Pantellini, F., & Moncuquet, M. 2016b, Planet. Space Sci., 120, 78
Varela, J., Pantellini, F., & Moncuquet, M. 2016c, Planet. Space Sci., 122, 46
Varela, J., Pantellini, F., & Moncuquet, M. 2016d, Planet. Space Sci., 125, 80
Varela, J., Reville, V., Brun, A. S., Pantellini, F., & Zarka, P. 2016e, A&A, 595, A69
Varela, J., Reville, V., Brun, A. S., Zarka, P., & Pantellini, F. 2018, A& A, 616, A182
Varela, J., Brun, A. S., Strugarek, A., et al. 2022a, A&A, 659, A10
Varela, J., Brun, A. S., Zarka, P., et al. 2022b, Space Weather, 20, e2022SW003164
Varela, J., Brun, A. S., Strugarek, A., et al. 2023, MNRAS, 525, 4008
Vedantham, H. K., Callingham, J. R., Shimwell, T. W., et al. 2020, Nat. Astron., 4, 577
Watanabe, M., Sakito, S., Tanaka, T., Shinagawa, H., & T., M. K. 2014, J. Geophys. Res.: Space Phys., 119, 6145
Waters, C. L., Anderson, B. J., & Liou, K. 2001, Geophys. Res. Lett., 28, 2165
Weimer, D. R. 2001, J. Geophys. Res.: Space Phys., 106, 12889
Wood, B. E., Linsky, J. L., Müller, H.-R., & Zank, G. P. 2001, ApJ, 547, L49
Wu, C. S., & Lee, L. 1979, ApJ, 230, 621
Yadav, R. K., Christensen, U. R., Wolk, S. J., & Poppenhaeger, K. 2016, ApJ, 833, L28
Zarka, P. 1998, J. Geophys. Res., 103, 20159
Zarka, P. 2007, Planet. Space Sci., 55, 598
Zarka, P. 2018, in Handbook of Exoplanets, eds. H. J. Deeg, & J. A. Belmonte, 22
Zarka, P., Marques, M. S., Louis, C., et al. 2018, A&A, 618, A84
Zhang, Q. H., Zhang, Y. L., Wang, C., et al. 2020, PNAS, 117, 16193
Zic, A., Murphy, T., Lynch, C., et al. 2020, ApJ, 905, 23

Appendix A: Upper ionosphere model

The upper ionospheric domain is located between $R = (2.2 - 2.5)\,R_E$. The upper ionosphere model is based on Büchner, J. et al. (2003). Below the lower boundary of the upper ionosphere, the magnetic field intensity is too high, thus the simulation time step is too small. In addition, a single-fluid MHD model cannot correctly reproduce magnetosphere regions such as the inner ionosphere or the plasma sphere because the kinetic effects are strong.

First, we calculate the field-aligned current (J_{FAC}) as

$$\boldsymbol{J_{FAC}} = \boldsymbol{J} - \boldsymbol{J_\perp}, \tag{A.1}$$

where

$$\boldsymbol{J} = \frac{1}{4\pi}\boldsymbol{\nabla} \times \boldsymbol{B} \tag{A.2}$$

$$\boldsymbol{J_\perp} = \boldsymbol{J} - \frac{J_r B_r + J_\theta B_\theta + J_\phi B_\phi}{|B|^2}\boldsymbol{B}, \tag{A.3}$$

with $\boldsymbol{J}$ the plasma current, $\boldsymbol{J_\perp}$ the perpendicular component of the plasma current along the magnetic field line, μ_0 the vacuum magnetic permeability, and $\boldsymbol{B}$ the magnetic field. Next, we compute the electric field of the upper ionosphere model using the Pedersen conductance (σ) empirical formula,

$$\sigma = \frac{40 E_0 \sqrt{F_E}}{16 + E_0^2}, \tag{A.4}$$

with $E_0 = k_B T_e$ the mean energy of the electrons, $F_E = n_e \sqrt{E_0/(2\pi m_e)}$ the energy flux, and k_B the Boltzmann constant (T_e and m_e are the electron temperature and mass, respectively). Thus, the electric field (E) linked to the FAC is

$$\boldsymbol{E} = \sigma \boldsymbol{J_{FAC}}. \tag{A.5}$$

Once we get the electric field, we compute the velocity of the plasma in the upper ionosphere using the standard relation

$$\boldsymbol{v} = \frac{\boldsymbol{E} \times \boldsymbol{B}}{|B|^2}. \tag{A.6}$$

We defined the plasma density in the upper ionosphere with respect to the Alfvén velocity. More specifically, we fixed the module of the Alfvén velocity, v_A, to control the simulation time step, so that the density profile, defined as

$$\rho = \frac{|B|^2}{4\pi\, v_A^2}. \tag{A.7}$$

did not evolve during the simulation between $R = (2.2 - 2.5)\,R_E$. We note that, while we kept fixed the value of v_A in each simulation, depending on the specific simulation this value could be different, as a result of the different values of the IMF and of the stellar wind density. The values of v_A ranged from $2.6 \cdot 10^4$ km/s to $5.0 \cdot 10^4$ km/s.

We defined the plasma pressure in the upper ionosphere model with respect to the sound speed of the stellar wind, c_{sw}, and at the inner boundary, c_p),

$$p = \frac{n}{\gamma}\left[\frac{(c_p - c_{sw})(r^3 - R_s^3)}{R_{un}^3 - R_s^3} + c_{sw}\right]^2, \tag{A.8}$$

with $\gamma = 5/3$ the polytropic index, $c_p = \sqrt{\gamma K_B T_p/m_p}$ with T_p the plasma temperature at the inner boundary, and $c_{sw} = \sqrt{\gamma K_B T_{sw}/m_p}$ with T_{sw} the stellar wind temperature.

We defined the initial model conditions of the plasma density and pressure so as to have a smooth transition between the upper ionosphere and the simulation domains. During the simulation, the pressure and density gradients increase because we kept fixed the density and pressure profiles inside the inner ionosphere, but evolved freely in the simulation domain. The reaction of the system during the early stages of the simulation is to feed plasma toward the simulation domain to compensate for the increase of the pressure and density gradients. This generates an outward plasma flux that saturates when the inner magnetosphere reaches a steady state. Henceforth, the plasma flows are driven by the balance between the stellar wind injection inside the inner magnetosphere, and the plasma streams toward the planet surface.

We note that the present model has been bench-marked against several codes, following the analysis performed by Samsonov et al. (2016), which was dedicated to the global structures of the Earth magnetosphere for quiet space weather conditions. Namely, we performed a simulation using the same parameters as in the original benchmark study: $n = 5$ cm^{-3}, $V_x = -400$ km/s, $T = 2 \cdot 10^5$ K, $B_y = -B_x = 35\,\mu$G , and $B_z = 0\,\mu$G . The location of the magnetopause is $R_x/R_E = 10.7$, $R_y/R_E = 16.8$, $R_{-y}/R_E = 16.6$, and $R_z/R_E = 14.9$. The model prediction and the benchmark study agree reasonably well. In addition, the electric field in the simulation domain is also consistent with the simulations in Samsonov et al. (2016) near the bow shock. The module of the electric field predicted inside the magnetosphere is similar to Cluster spacecraft observations during the magnetopause crossing on 30/02/2002 (De Keyser et al. 2005). The electric field measured in the current sheet and magnetosheath is an order of magnitude higher than the simulations because the IMF module is 10 times larger during the Cluster magnetopause crossing. When the simulation was performed using a southward IMF with $|B| = 500\,\mu$G and $P_d = 5$ nPa, similar to the space weather conditions during Cluster magnetopause crossing, the predicted electric field is 15 − 30 mV/m in the current sheet and magnetosheath region. This is similar to Cluster spacecraft observations.

We also performed another two simulations using the same SW parameters, but for northward and southward IMF orientations with $|B_z| = 3$ nT, identifying the displacement of the magnetopause location defined as $\Delta R/R_E$ = northward$(R)/R_E$ − southward$(R)/R_E$: $\Delta R_x/R_E = 0.2$, $\Delta R_y/R_E = 0.1$ and $\Delta R_z/R_E = -1.0$. As in the previous case, we also found reasonable agreement with the benchmark case.

Next, we compared that model with the Carrington-like event analysed by Ridley et al. (2006), who identified a magnetopause standoff distance of $R/R_E = 2$ (equal to the lower boundary of the simulation domain) for the parameters $n = 750$ cm^{-3}, $V_x = -1600$ km/s ($P_d = 1600$ nPa), $T = 3.5 \cdot 10^7$ K, $B_x = 1.5$ mG, $B_y = 1.7$ mG, and $B_z = 2.0$ mG. This model cannot be used to simulate space weather conditions leading to a magnetopause standoff distance smaller $R/R_E = 2.5$, although the extrapolation of the model results predicts $R/R_E \approx 1.22$ if $P_d = 1600$ nPa and $B_z = 2.0$ mG (pure southward IMF orientation).

Finally, we note that the electric field in the upper ionosphere domain remains almost unchanged during the simulation because we had fixed the density profile. The radial electric field inside the upper ionosphere (northern hemisphere at $R/R_E = 3.1$) shows a reasonable agreement with respect to other

models and satellite measurements (Shume et al. 2009; Watanabe et al. 2014).

FAC intensity and orientation values are in the range of the observations and modeling data (from nA/m^2 to several μAm^2 regarding space weather conditions) (Weimer 2001; Waters et al. 2001; Ritter et al. 2013; Bunescu et al. 2019; Zhang et al. 2020)

Appendix B: Calculation of the radio emission from the interaction regions

We calculated the power dissipated in the interaction regions between the stellar wind and the magnetosphere at the exoplanet dayside, using Eq. 6. In the (calm weather) sub-Alfvénic scenario, no bow shock is formed, so the only region contributing to the radio emission is the magnetopause. In the super-Alfvénic case (both under calm space weather conditions, or under more extreme, CME-like conditions), a bow shock is also formed, so there are two regions contributing to the dissipation of the deposited energy.

To perform those calculations, we defined the integration regions as accurately as possible. For example, the magnetopause emission takes place around the reconnection region. We excluded the magneto-tail zone from it, as it was not included in the numerical modeling. Also, we put special care, so that the integration region did not fall too close to the planet, as this could cause artificial emission near the boundaries of the simulation. In the cases when a bow shock is formed, the integration region coves all the space with high density, arising from the collision of the stellar wind with the magnetic field of the planet. We ensured that the inner boundary was similar to the outer boundary of the magnetopause, so as to avoid overlapping emission.

We illustrate in Fig. B.1 the different contributions from the bow shock and the magnetopause for a super-Alfvénic case, after having carried out the steps outlined.

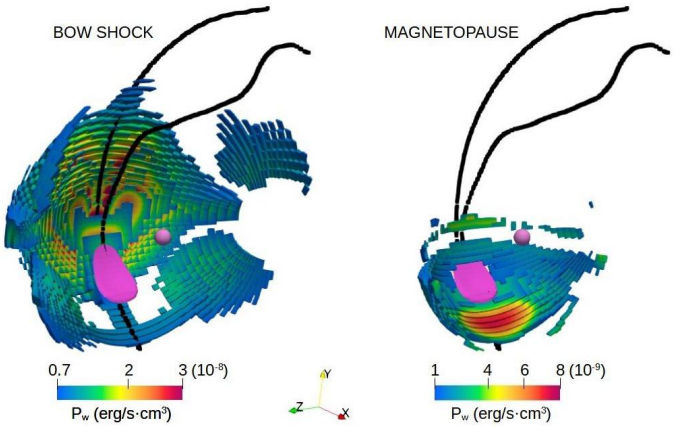

Fig. B.1: Contribution to the radio emission from the bow shock (left) and magnetopause (right) regions for one of our simulations. The black solid lines indicate the bow shock position, and the area colored in purple represents the magnetic reconnection region.